

Flexible radio-frequency transistors exceeding 100 GHz

Fan Xia^{1†}, Tian Xia^{1,3†}, Haotian Su^{2†}, Lanyue Gan¹, Qianlan Hu¹, Wanyi Wang¹, Ruyi Huang^{1,3}, Tianshun Bai¹, Yufan Chen¹, Chao Ma¹, Guanhua Long¹, Shan X. Wang², Eric Pop^{2*}, Lian-Mao Peng^{1,3*}, Youfan Hu^{1,3*}

¹Key Laboratory for the Physics and Chemistry of Nanodevices, Center for Carbon-Based Electronics, and School of Electronics, Peking University; Beijing 100871, China.

²Department of Electrical Engineering, Stanford University; Stanford, CA 94305, USA.

³Academy for Advanced Interdisciplinary Studies, Peking University; Beijing 100871, China.

†These authors contributed equally to this work.

*Corresponding author. Email: epop@stanford.edu, lmpeng@pku.edu.cn, youfanhu@pku.edu.cn.

The advent of 6G communication demands seamlessly integrated terminals operating above 100 GHz with low power consumption for human-centric applications. In this work, we report high-performance, flexible radio-frequency (RF) transistors based on aligned carbon nanotube (CNT) arrays, achieving, for the first time, as-measured current gain cutoff frequency (f_T) and power gain cutoff frequency (f_{max}) both exceeding 100 GHz. Electro-thermal co-design improves both heat dissipation and RF performance, despite the low thermal conductivity of the flexible substrate. The transistors deliver 0.947 mA/ μ m on-state current and 0.728 mS/ μ m transconductance. Peak extrinsic f_T and f_{max} reach 152 GHz and 102 GHz, with low power consumption of 199 mW/mm and 147 mW/mm, respectively, setting new performance records for flexible CNT-based RF transistors by nearly 100 \times , outperforming all other flexible RF devices. Additionally, flexible RF amplifiers achieve output power of 64 mW/mm and power gain of 11 dB in the K-band (18 GHz), marking a significant milestone in the development of flexible RF technologies for next-generation wireless communication systems.

The coming 6G communication technology, expected in the 2030s, aims to deliver ultrahigh data transmission rates exceeding 100 gigabits per second. This advancement requires significantly wider bandwidths and operations at higher frequencies within terahertz (THz) range, spanning 0.1 THz to 10 THz (1-5). A key feature of the 6G technology is its focus on ubiquitously connected, human-centric communications, enabling new application scenarios such as holographic communications, tactile internet, and extended reality. These technologies will allow access to and/or sharing of human senses and enable remote interactions with the human body (5-7). New communication terminals capable of collecting biological features, monitoring physiological indexes, detecting emotions, and replicating human senses (8, 9), are critical enablers of these innovative communication forms. Owing to their light weight, biocompatibility, adaptability and convenience (10), flexible wireless terminals operating at frequencies over 100 gigahertz (GHz) with low power consumption toward seamless integration are ideal for human-centric 6G applications, where flexible radio-frequency (RF) transistors serve as key components. Among previously reported flexible RF transistors based on III-V semiconductors (11-13), organic materials (14), amorphous oxide semiconductors (15, 16), and two-dimensional (2D) materials (17-19), those based on III-V semiconductors (e.g., GaN and GaAs) typically offer the highest performance, with a reported extrinsic current-gain cutoff frequency (f_T) of up to 42 GHz (12). However, building flexible RF transistors capable of operating beyond 100 GHz for 6G applications remains a significant challenge.

Carbon nanotubes (CNTs) are regarded as promising candidates for building next-generation integrated

circuits (20, 21). It is theoretically estimated that CNT-based transistors have the potential to work in the THz regime due to the high saturation velocity, ultrasmall intrinsic capacitance, excellent thermal conductivity and stability of CNTs (22-24). Previous studies of CNT-based RF transistors on rigid substrates have demonstrated a high extrinsic f_T of 186 GHz (25). In addition, unlike RF transistors based on III–V semiconductors, CNT-based RF transistors offer easier integration with digital and analog circuits based on the same materials, a critical advantage for system-on-chip technology (26). Moreover, CNTs' moderate band gaps enable low-power operation (21), facilitating seamless integration with biointerfaces. However, the highest reported f_T of flexible CNT-based RF transistors is only 2 GHz (27), which is far below their theoretical potential, highlighting substantial room for improvement.

Herein, we present high-performance flexible RF transistors based on aligned CNT arrays, designed with electro-thermal co-optimization on flexible polyimide (PI) substrates. These transistors achieve extrinsic f_T and power-gain cutoff frequency (f_{max}) values of 152 GHz and 102 GHz, respectively, surpassing previously reported flexible RF transistors based on various materials. They also demonstrate low power consumption, with direct current (DC) power as low as 199 mW/mm and 147 mW/mm, correspondingly. Leveraging these high-performance RF transistors, we further demonstrate flexible RF power amplifiers operating at 18 GHz, achieving a gain of 11 dB and an output power of 64.45 mW/mm. These advancements hold great promise for enabling next-generation human-centric 6G applications.

Device Structure and DC Performance

Human-centric communication in the 6G technology envisions multiple seamlessly integrable terminals bonded to the human body for information collection, sharing, and communication, as illustrated in Fig. 1A. The structure of our RF transistors based on aligned CNTs arrays is depicted in Fig. 1B, where the transistors are fabricated on a flexible polyimide (PI) substrate with a thickness of 2 μm . The design incorporates a two-finger, top-gated architecture with air gaps between the gate and source/drain contacts to reduce parasitic effects. Owing to its low dielectric loss, high glass temperature, relatively high thermal conductivity (among flexible polymer substrates) (28, 29), the PI substrate is selected to meet the stringent requirements of RF applications. Its low surface roughness, achieved via spin-coating, facilitates the fabrication of high-performance devices. Aligned CNT arrays were deposited on a silicon wafer via a dimension-limited self-alignment procedure (25, 30) and then transferred to the PI substrate. Palladium (Pd) was chosen as the contact metal to form ohmic contacts with the CNTs (30, 31). The entire fabrication process is provided in fig. S1.

Scaling down the channel length (L_{ch}) is an effective way to promote transistor performance (31, 32). Moreover, achieving impedance matching between the transistor and the measurement system requires a large channel width, while minimizing parasitic capacitance necessitates air gaps between the gate and the source/drain contacts. To meet these requirements, the gate electrode must possess a high width-to-length ratio and be precisely aligned at the center of the downscaled channel. To address these challenges, we optimized the fabrication process on the flexible substrate, achieving a gate length (L_g) down to 75 nm. Each finger of the two-finger device features a channel width of 10 μm , resulting in a width-to-length ratio of 133:1. Figure 1C shows scanning electron microscopy (SEM) images of the fabricated flexible RF transistors. In the enlarged view at the bottom, the 75 nm-long gate is well-aligned at the center of the 120 nm-long channel. The SEM image of the aligned CNT arrays on the flexible substrate is shown in fig. S2, demonstrating a high density of approximately 150 CNTs/ μm and a good uniformity.

The transfer and output characteristics of a typical flexible RF transistor with an L_g of 75 nm and an L_{ch} of 120 nm are presented in Fig. 1, D and E. The device exhibits excellent DC performance, achieving an on-state current (I_{on}) of 0.947 mA/ μ m and a transconductance (g_m) of 0.728 mS/ μ m. These values are comparable to those achieved in aligned CNT array-based RF transistors on rigid substrates under similar bias conditions (25). The intrinsic f_T ($f_{T, int}$) is theoretically proportional to g_m (22, 33, 34), indicating the importance of a large g_m in DC performance for achieving superior RF performance in flexible RF transistors. Compared with other high-performance flexible transistors based on various materials (13-15, 18, 19, 32, 35, 36), as shown in Fig. 1F, our devices demonstrate the highest I_{on} and g_m at supply voltage no more than 0.6 V. This highlights their application potential for high-performance and low-power electronics.

Electro-Thermal Co-Design

Achieving very high current densities is often challenging for downscaled transistors due to significant self-heating, which presents a critical bottleneck to performance and reliability(37, 38). This issue is particularly pronounced in flexible devices with polymer-based substrates, which have low thermal conductivity (35, 39). The breakdown temperature of CNTs in air (38, 40) is approximately 600 °C, while the glass transition temperature of the PI substrate is approximately 350 °C, with a decomposition temperature (29) of nearly 500 °C. To assess the thermal constraints imposed by the flexible substrate, we conducted finite-element electro-thermal simulations (35) to compare the temperature profiles of an electrically optimized CNT-based RF transistor (25) operating at the same power on a rigid quartz substrate and a flexible PI substrate. As shown in fig. S3, the transistor operates well below its breakdown temperature on the rigid substrate. However, on the PI substrate, the maximum temperatures of the CNTs and the PI substrate reached 627 °C and 341 °C, respectively, exceeding or approaching their breakdown limits. These findings highlight that, on flexible substrates, the high performance of RF devices requires not only the superior material properties of the aligned CNT arrays, but it is also essential to limit their self-heating by reducing power consumption and implementing effective thermal management strategies.

We employed electro-thermal co-design for flexible RF transistors to achieve high RF performance and low power consumption, while maintaining a well-controlled temperature rise (ΔT). For transistors on flexible substrates with low thermal conductivity, heat dissipation through the contacts becomes critical (35). Thicker metal contacts aid heat dissipation both due to higher thermal conductance (larger area for heat flow) and higher thermal conductivity (less boundary scattering) (41), while thinner contacts minimize parasitic capacitances between source/drain and gate, for high-speed performance. To balance these requirements, a contact stack of 20 nm palladium (Pd) and 20 nm gold (Au) was employed (Fig. 2A), where Pd forms good ohmic contact with CNTs, and Au improves thermal and electrical conductance. The gate was similarly engineered using an Al₂O₃/Al/Ti/Au stack to minimize thermal resistance and provide an additional heat dissipation pathway. Al₂O₃ was selected as the gate dielectric for its higher thermal conductivity than HfO₂ (42), with an Al layer directly deposited on top to achieve a thermal boundary conductance (TBC) (43) of ~ 200 MWm⁻²K⁻¹, significantly better than expected for Au/Al₂O₃ interfaces with a TBC of ~ 20 MWm⁻²K⁻¹. A thin Ti layer was introduced between Al and Au to prevent the formation of Au-Al intermetallic, which may introduce thermal and electrical instability (44). To further optimize heat dissipation, the total gate stack thickness was set to 190 nm, ensuring near-bulk metal thermal conductivity (41) while simultaneously reducing gate resistance for improved RF performance.

The heat map in Fig. 2A illustrates the calculated ΔT of the flexible RF transistor with $L_g = 75$ nm under working conditions, showing a maximum ΔT of 331 °C for the CNT channel and 168 °C for the flexible substrate. (Thermal analysis details are provided in Supplementary Text.) In the zoomed-in, top-down view of the channel (Fig. 2B, top), the temperature profile appears uniform across its width direction, with significant temperature drops at the source and drain contacts. As shown in the ΔT profile along the channel (Fig. 2B, bottom), the temperature decays with a characteristic thermal healing length ($L_H \approx 300$ nm), which is much longer than that on rigid substrates with better heat-sinking properties (e.g., doped Si). This underscores the critical role of source and drain contacts for lateral heat dissipation, suggesting that the CNT contact (L_{ch}) length should ideally exceed L_H .

We evaluated the maximum ΔT of flexible RF transistors with L_g ranging from 75 nm to 420 nm, as summarized in Fig. 2C. Across all devices, the ΔT of the CNTs and the flexible substrate remain below 360 °C and 200 °C, respectively. The maximum ΔT shows slight variations corresponding to changes in DC power ($P_{dc} = I_d V_{ds}$ during the scattering (S) parameter measurements), as listed in fig. S4C. All L_{ch} here are relatively short, $L_{ch} < 3L_H$ (with L_{ch} ranging from 120 to 540 nm), which explains why the thermal resistance of our devices does not scale with L_{ch} (45). This is reflected in Fig. 2C where the peak temperature is relatively constant (at relatively constant power) despite the channel length increasing by $> 4\times$. For longer channel devices ($L_{ch} > 3L_H$) or devices on silicon (where L_H is much shorter), one would expect the peak temperature to scale inversely with the channel length, given the same power, because the power density (per channel area) would reduce. These results confirm that, with our optimized device design for heat dissipation, the CNT channel operates well below its breakdown temperature, while the maximum temperature of the PI substrate remains safely below its glass transition temperature. In principle, our devices could sustain even higher P_{dc} , offering the potential for higher RF performance without thermal degradation.

RF Performance

Figure 2D shows the relationship between the current gain and frequency for a flexible transistor with a L_g of 75 nm under small-signal measurements at an input power of -10 dBm, extracted from the measured two-port S-parameters, as shown in fig. S5. The extrinsic (as-measured) f_T ($f_{T,ext}$) of the device reaches 152 GHz, falling within the sub-THz regime (100 GHz to 300 GHz). After performing a standard pad de-embedding procedure (more details in Supplementary Text and fig. S6), the pad de-embedding f_T ($f_{T,pad}$) reaches 171 GHz, with a low de-embedding ratio ($f_{T,pad}/f_{T,ext}$) of 1.125, indicating minimal parasitic effects from the substrate and the measurement setup. The intrinsic de-embedding further eliminates the parasitic effects from the device structure itself, revealing the intrinsic material properties (19, 25). This yields an intrinsic f_T ($f_{T,int}$) of 310 GHz, which enters the THz regime (300 GHz to 3 THz), and is comparable to the $f_{T,int}$ obtained from RF transistors based on aligned CNT arrays on silicon wafer with similar gate lengths ($L_g = 60$ nm, $f_{T,int} = 365$ GHz; $L_g = 90$ nm, $f_{T,int} = 238$ GHz) (25). This demonstrates that the aligned CNT arrays retain their superior properties after being transferred from the silicon wafer to the PI substrate.

Figure 2E presents the small-signal power gains as a function of frequency for a flexible transistor with $L_g = 160$ nm. The extrinsic f_{max} ($f_{max,ext}$) maximizes in this device, reaching 102 GHz. After pad de-embedding and intrinsic de-embedding, the f_{max} reaches 141 GHz ($f_{max,pad}$) and 168 GHz ($f_{max,int}$), respectively. Figure 2F shows $f_{T,ext}$ under varying bias conditions (V_{gs} and V_{ds}). A higher V_{ds} offers higher $f_{T,ext}$, while the optimal V_{gs} (approximately -0.5 V) corresponds to the V_{gs} that maximum g_m in the DC performance (Fig. 1D). The optimized bias conditions for achieving the highest $f_{max,ext}$, $f_{T,pad}$, $f_{max,pad}$ are

summarized in fig. S7.

To investigate the scaling behavior, the extrinsic current gains and power gains of flexible RF transistors with six different L_g ranging from 75 nm to 420 nm are shown in Fig. 3, A and B, respectively, while the pad de-embedded and intrinsic current gains and power gains are presented in fig. S8. Figure 3C illustrates the relationship between f_T (extrinsic, pad de-embedded, and intrinsic) and L_g . Both the extrinsic and pad de-embedded f_T increase as L_g decreases, while the intrinsic f_T shows inversely proportionality to L_g , consistent with the small signal model ($f_{T,int} = g_m/(2\pi C_g) = g_m/(2\pi C_{ox}WL_g) \propto 1/L_g$, where C_g is the gate capacitance, C_{ox} is the gate capacitance per unit area and W is the channel width) (22, 46). Figure 3D depicts the variations in f_{max} (extrinsic, pad de-embedded, and intrinsic) with L_g . Notably, f_{max} peaks at $L_g = 160$ nm and decreases as L_g further decreases, which may result from the rapid increase in gate resistance for devices with shorter L_g (25, 46).

Figure 3E shows the extracted de-embedding ratios from Fig. 3, C and D, which are defined as the ratio of the de-embedded to the corresponding extrinsic f_T or f_{max} . The pad de-embedding ratios remain below 1.2 for f_T and 1.4 for f_{max} during L_g scaling. We measured the two-port S-parameters of the pad de-embedding structures on the PI substrate, with the results shown as Smith charts in fig. S9. The S_{11} and S_{22} parameters of the open structure are very close to the infinite impedance point with negligible frequency dispersion. This finding indicates that the high frequency loss from the PI substrate is very low, supporting the low pad de-embedding ratios achieved in these devices. The intrinsic de-embedding ratio of f_T increases as L_g decreases, with more pronounced changes when L_g scales down to sub-200 nm. This indicates that the parasitic effects from the device structure itself become dominant at smaller dimensions, requiring further structure optimization to fully leverage the superior material properties for higher f_T . Figure 3F shows the statistical distributions of the $f_{T,ext}$ for flexible RF transistors with different L_g , while the $f_{max,ext}$, $f_{T,pad}$ and $f_{max,pad}$ distributions are provided in fig. S10. The average values and standard variations of f_T and f_{max} are summarized in table S1. Specifically, the $f_{T,ext}$ distribution for flexible RF transistors with $L_g = 75$ nm is 141.17 ± 9.2 GHz, while the $f_{max,ext}$ distribution of flexible RF transistors with $L_g = 160$ nm is 92.34 ± 9.23 GHz, demonstrating good uniformity and high performance across the fabricated devices.

Performance Benchmarking

The performance and power consumption of our flexible RF transistors are benchmarked with other flexible RF transistors. As shown in Fig. 4A, our devices achieve the highest $f_{T,ext}$ of 152 GHz compared to other state-of-the-art flexible RF transistors based on various materials, including conventional III-IV semiconductors (12), amorphous oxide semiconductors (15, 16), 2D materials (17-19), organic materials (14) and other CNTs (27). Remarkably, this $f_{T,ext}$ is 95 times higher than that of previously reported flexible RF transistors based on CNT materials (27) and approximately 3 times higher than that of flexible RF transistors based on III-V materials (12). Furthermore, our devices achieve the highest $f_{max,ext}$ of 102 GHz, surpassing the $f_{max,ext}$ of flexible RF transistors based on III-IV materials (12) and more than 6 times that of flexible RF transistors based on other materials (14-19). These results, for the first time, demonstrate both $f_{T,ext}$ and $f_{max,ext}$ exceeding 100 GHz in flexible RF transistors, a significant milestone for 6G applications. Figure 4B shows the $f_{T,ext}$ versus $f_{max,ext}$ for these benchmarked works, with the geometric mean value $(f_{T,ext} \times f_{max,ext})^{1/2}$, a balanced indicator of high frequency performance of RF transistors) of our devices reaching 106 GHz, which is twice the highest value of flexible RF transistors based on III-IV materials (12).

Low power consumption is another critical requirement for communication terminals. Compared to

other flexible RF transistors that typically operate at a supply voltage above 1.5 V (11, 12, 14, 17-19, 27), our devices achieve an $f_{T,\text{ext}}$ of 152 GHz under a V_{ds} of 0.65 V and an $f_{\text{max,ext}}$ of 102 GHz under a V_{ds} of 1.05 V, as shown in Fig. 4C, showcasing significantly higher performance with lower power consumption. As illustrated in Fig. 4D, the $f_{T,\text{ext}}$ and $f_{\text{max,ext}}$ versus the P_{dc} are also benchmarked, with P_{dc} values of 199 mW/mm and 147 mW/mm for the highest $f_{T,\text{ext}}$ and $f_{\text{max,ext}}$, respectively. These values outperform those of flexible RF transistors based on other materials (11, 12, 18, 19, 27) and are even lower than those of their rigid counterparts based on aligned CNTs with similar performance (25, 47, 48). These results highlight the potential of our devices for energy-efficient, high-performance flexible RF applications.

Flexibility Assessment and RF Amplifier Performance

Flexibility tests were performed by bending the flexible substrate to various curvatures, followed by device characterization after release. Figure 5A shows the current gains of a typical RF transistor with $L_g = 200$ nm after bending to different radii of curvature, along with the changes in $f_{T,\text{ext}}$ versus the bending radius. The $f_{T,\text{ext}}$ was 54 GHz before bending and remained above 50 GHz after bending to a curvature radius of 1.5 mm. Figure 5B shows the measured current gains and the changes in $f_{T,\text{ext}}$ of the RF transistor after multiple bending cycles at a curvature radius of 3 mm. After 1000 bending cycles, $f_{T,\text{ext}}$ decreases slightly by 8% to 49.6 GHz, demonstrating good mechanical resilience.

A flexible RF power amplifier was constructed based on these RF transistors with $L_g = 160$ nm, incorporating 6 fingers to increase the channel width and achieve impedance match. Figure 5C represents the output power (P_{out}) and the power gain of the flexible RF power amplifier versus the input power (P_{in}) at a working frequency (f_0) of 18 GHz (in the K band). The amplifier achieves a P_{out} of 64 mW/mm and a maximum power gain of 11 dB. Figure 5D shows the drain efficiency (DE) and the power-added efficiency (PAE) of the flexible RF power amplifier versus P_{in} , with DE peaking at 18% and PAE at 10%. Our flexible RF power amplifier has good performance when it works under a f_0 of 18 GHz, which shows the potential to build flexible RF circuits and communication systems with high frequencies.

Discussion

In conclusion, we fabricated high-performance flexible RF transistors based on aligned CNT arrays, achieving both $f_{T,\text{ext}}$ and $f_{\text{max,ext}}$ values exceeding 100 GHz. Through electro-thermal co-design, we optimized the devices for high RF performance and greatly enhanced heat dissipation. Our flexible transistors achieve an I_{on} of 0.947 mA/ μm and a g_m of 0.728 mS/ μm , demonstrating the highest extrinsic f_T of 152 GHz and f_{max} of 102 GHz among all reported flexible RF transistors. These devices also exhibit low power consumption below 200 mW/mm, alongside excellent flexibility. Furthermore, a flexible RF power amplifier fabricated from these transistors achieves a P_{out} of 64 mW/mm and a power gain of 11 dB at a f_0 of 18 GHz.

This work marks the first time the operating frequencies of flexible RF transistors have surpassed 100 GHz, demonstrating that CNT materials are highly competitive for building high-performance RF devices on flexible substrates. Our findings also highlight opportunities for further advancements in areas such as substrate engineering, device design and system integration. Optimizing flexible substrates to achieve higher thermal conductivity and lower dielectric loss is particularly critical, while electro-thermal co-design proves effective in simultaneously reducing parasitic effects and enhancing heat dissipation efficiency. Being integrated with flexible sensors, flexible CNT-based digital/analog ICs and

antennas, CNT-based flexible RF circuits with high speed and low power show great promise for enabling seamlessly integrable, human-bond communication terminals in the next-generation 6G technology.

References and Notes:

1. T. S. Rappaport *et al.*, Wireless communications and applications above 100 GHz: Opportunities and challenges for 6G and beyond. *IEEE Access* **7**, 78729-78757 (2019).
2. I. F. Akyildiz, A. Kak, S. Nie, 6G and beyond: The future of wireless communications systems. *IEEE Access* **8**, 133995-134030 (2020).
3. W. Saad, M. Bennis, M. Chen, A vision of 6G wireless systems: Applications, trends, technologies, and open research problems. *IEEE Network* **34**, 134-142 (2020).
4. H. Tataria *et al.*, 6G wireless systems: Vision, requirements, challenges, insights, and opportunities. *Proc. IEEE* **109**, 1166-1199 (2021).
5. S. Dang, O. Amin, B. Shihada, M.-S. Alouini, What should 6G be? *Nat. Electron.* **3**, 20-29 (2020).
6. M. Alsabab *et al.*, 6G wireless communications networks: A comprehensive survey. *IEEE Access* **9**, 148191-148243 (2021).
7. E. Calvanese Strinati *et al.*, 6G: The next frontier: From holographic messaging to artificial intelligence using subterahertz and visible light communication. *IEEE Veh. Technol. Mag.* **14**, 42-50 (2019).
8. S. Liu, Y. Rao, H. Jang, P. Tan, N. Lu, Strategies for body-conformable electronics. *Matter* **5**, 1104-1136 (2022).
9. Y. Dai, H. Hu, M. Wang, J. Xu, S. Wang, Stretchable transistors and functional circuits for human-integrated electronics. *Nat. Electron.* **4**, 17-29 (2021).
10. L. Xiang *et al.*, Recent advances in flexible and stretchable sensing systems: From the perspective of system integration. *ACS Nano* **14**, 6449-6469 (2020).
11. Y. H. Jung *et al.*, High-performance green flexible electronics based on biodegradable cellulose nanofibril paper. *Nat. Commun.* **6**, 7170 (2015).
12. N. R. Glavin *et al.*, Flexible gallium nitride for high-performance, strainable radio-frequency devices. *Adv. Mater.* **29**, 1701838 (2017).
13. S. Mhedhbi *et al.*, First power performance demonstration of flexible AlGaIn/GaN high electron mobility transistor. *IEEE Electron Device Lett.* **37**, 553-555 (2016).
14. J. W. Borchert *et al.*, Flexible low-voltage high-frequency organic thin-film transistors. *Sci. Adv.* **6**, eaaz5156 (2020).
15. Q. Hu *et al.*, Ultrashort 15-nm flexible radio frequency ITO transistors enduring mechanical and temperature stress. *Sci. Adv.* **8**, eade4075 (2022).
16. N. Münzenrieder, G. Cantarella, L. Petti, Fabrication and ac performance of flexible indium-gallium-zinc-oxide thin-film transistors. *ECS Trans.* **90**, 55-63 (2019).
17. Q. Gao *et al.*, Scalable high performance radio frequency electronics based on large domain bilayer MoS₂. *Nat. Commun.* **9**, 4778 (2018).
18. W. Wei *et al.*, Mechanically robust 39 GHz cut-off frequency graphene field effect transistors on flexible substrates. *Nanoscale* **8**, 14097-14103 (2016).

19. W. Zhu *et al.*, Black phosphorus flexible thin film transistors at gighertz frequencies. *Nano Lett.* **16**, 2301-2306 (2016).
20. W. Cao *et al.*, The future transistors. *Nature* **620**, 501-515 (2023).
21. L.-M. Peng, Z. Zhang, C. Qiu, Carbon nanotube digital electronics. *Nat. Electron.* **2**, 499-505 (2019).
22. P. J. Burke, AC performance of nanoelectronics: Towards a ballistic THz nanotube transistor. *Solid-State Electron.* **48**, 1981-1986 (2004).
23. J. Guo, S. Hasan, A. Javey, G. Bosman, M. Lundstrom, Assessment of high-frequency performance potential of carbon nanotube transistors. *IEEE Trans. Nanotechnol.* **4**, 715-721 (2005).
24. S. O. Koswatta, A. Valdes-Garcia, M. B. Steiner, Y.-M. Lin, P. Avouris, Ultimate RF performance potential of carbon electronics. *IEEE Trans. Microwave Theory Tech.* **59**, 2739-2750 (2011).
25. H. Shi *et al.*, Radiofrequency transistors based on aligned carbon nanotube arrays. *Nat. Electron.* **4**, 405-415 (2021).
26. R. Saleh *et al.*, System-on-chip: Reuse and integration. *Proc. IEEE* **94**, 1050-1069 (2006).
27. Y. Lan *et al.*, High-temperature-annealed flexible carbon nanotube network transistors for high-frequency wearable wireless electronics. *ACS Appl. Mater. Interfaces* **12**, 26145-26152 (2020).
28. D.-J. Liaw *et al.*, Advanced polyimide materials: Syntheses, physical properties and applications. *Prog. Polym. Sci.* **37**, 907-974 (2012).
29. C. E. Sroog, Polyimides. *Prog. Polym. Sci.* **16**, 561-694 (1991).
30. L. Liu *et al.*, Aligned, high-density semiconducting carbon nanotube arrays for high-performance electronics. *Science* **368**, 850-856 (2020).
31. Y. Lin *et al.*, Scaling aligned carbon nanotube transistors to a sub-10 nm node. *Nat. Electron.* **6**, 506-515 (2023).
32. G. Long *et al.*, Carbon nanotube-based flexible high-speed circuits with sub-nanosecond stage delays. *Nat. Commun.* **13**, 6734 (2022).
33. D. Krasnozhan, D. Lembke, C. Nyffeler, Y. Leblebici, A. Kis, MoS₂ transistors operating at gigahertz frequencies. *Nano Lett.* **14**, 5905-5911 (2014).
34. F. Schwierz, Graphene transistors. *Nat. Nanotechnol.* **5**, 487-496 (2010).
35. A. Daus *et al.*, High-performance flexible nanoscale transistors based on transition metal dichalcogenides. *Nat. Electron.*, 495-501 (2021).
36. N. Münzenrieder *et al.*, Focused ion beam milling for the fabrication of 160 nm channel length IGZO TFTs on flexible polymer substrates. *Flexible Printed Electron.* **5**, 015007 (2020).
37. S. V. Garimella *et al.*, Thermal challenges in next-generation electronic systems. *IEEE Trans. Compon. Packag. Technol.* **31**, 801-815 (2008).
38. E. Pop, Energy dissipation and transport in nanoscale devices. *Nano Res.* **3**, 147-169 (2010).
39. J. Yun, Recent progress in thermal management for flexible/wearable devices. *Soft Sci.* **3**, 12 (2023).
40. E. Pop, D. A. Mann, K. E. Goodson, H. Dai, Electrical and thermal transport in metallic single-wall carbon nanotubes on insulating substrates. *J. Appl. Phys.* **101**, 093710 (2007).
41. J. M. Lugo, A. I. Oliva, Thermal properties of metallic films at room conditions by the heating slope. *J. Thermophys. Heat Transfer* **30**, 452-460 (2016).

42. E. A. Scott, J. T. Gaskins, S. W. King, P. E. Hopkins, Thermal conductivity and thermal boundary resistance of atomic layer deposited high-k dielectric aluminum oxide, hafnium oxide, and titanium oxide thin films on silicon. *APL Mater.* **6**, 058302 (2018).
43. J. Paterson, D. Singhal, D. Tainoff, J. Richard, O. Bourgeois, Thermal conductivity and thermal boundary resistance of amorphous Al₂O₃ thin films on germanium and sapphire. *J. Appl. Phys.* **127**, 245105 (2020).
44. E. Philofsky, Intermetallic formation in gold-aluminum systems. *Solid-State Electron.* **13**, 1391-1394 (1970).
45. A. J. Gabourie, Ç. Köroğlu, E. Pop, Substrate-dependence of monolayer MoS₂ thermal conductivity and thermal boundary conductance. *J. Appl. Phys.* **131**, 195103 (2022).
46. D. Zhong, Z. Zhang, L. M. Peng, Carbon nanotube radio-frequency electronics. *Nanotechnology* **28**, 212001 (2017).
47. C. Rutherglen *et al.*, Wafer-scalable, aligned carbon nanotube transistors operating at frequencies of over 100 GHz. *Nat. Electron.* **2**, 530-539 (2019).
48. Y. Cao *et al.*, Radio frequency transistors using aligned semiconducting carbon nanotubes with current-gain cutoff frequency and maximum oscillation frequency simultaneously greater than 70 GHz. *ACS Nano* **10**, 6782-6790 (2016).
49. R. Prasher, Thermal interface materials: Historical perspective, status, and future directions. *Proc. IEEE* **94**, 1571-1586 (2006).
50. Ç. Köroğlu, E. Pop, High thermal conductivity insulators for thermal management in 3D integrated circuits. *IEEE Electron Device Lett.* **44**, 496-499 (2023).
51. K. M. Razeeb, E. Dalton, G. L. W. Cross, A. J. Robinson, Present and future thermal interface materials for electronic devices. *Int. Mater. Rev.* **63**, 1-21 (2018).
52. A. A. Balandin, Thermal properties of graphene and nanostructured carbon materials. *Nat. Mater.* **10**, 569-581 (2011).
53. B. Kumaneck, D. Janas, Thermal conductivity of carbon nanotube networks: A review. *J. Mater. Sci.* **54**, 7397-7427 (2019).
54. A. M. Marconnet, M. A. Panzer, K. E. Goodson, Thermal conduction phenomena in carbon nanotubes and related nanostructured materials. *Rev. Mod. Phys.* **85**, 1295-1326 (2013).
55. G. D. Mahan, M. Bartkowiak, Wiedemann–franz law at boundaries. *Appl. Phys. Lett.* **74**, 953-954 (1999).
56. M. Jonson, G. D. Mahan, Mott's formula for the thermopower and the wiedemann-franz law. *Phys. Rev. B* **21**, 4223-4229 (1980).
57. A. N. Volkov, L. V. Zhigilei, Scaling laws and mesoscopic modeling of thermal conductivity in carbon nanotube materials. *Phys. Rev. Lett.* **104**, 215902 (2010).
58. A. Javey *et al.*, High-field quasiballistic transport in short carbon nanotubes. *Phys. Rev. Lett.* **92**, 106804 (2004).
59. Y. Zhang, H. Dai, Formation of metal nanowires on suspended single-walled carbon nanotubes. *Appl. Phys. Lett.* **77**, 3015-3017 (2000).
60. Z. Chen, J. Appenzeller, J. Knoch, Y. M. Lin, P. Avouris, The role of metal-nanotube contact in the performance of carbon nanotube field-effect transistors. *Nano Lett.* **5**, 1497-1502 (2005).
61. M. Asheghi, M. N. Touzelbaev, K. E. Goodson, Y. K. Leung, S. S. Wong, Temperature-dependent thermal conductivity of single-crystal silicon layers in SOI substrates. *J. Heat Transfer* **120**, 30-36 (1998).
62. E. Yalon *et al.*, Energy dissipation in monolayer MoS₂ electronics. *Nano Lett.* **17**, 3429-3433 (2017).

63. T. Laumer *et al.*, Fundamental investigation of laser beam melting of polymers for additive manufacture. *J. Laser Appl.* **26**, 042003 (2014).
64. J. Dong, L. Cao, Y. Li, Z. Wu, C. Teng, Largely improved thermal conductivity of PI/BNNS nanocomposites obtained by constructing a 3D BNNS network and filling it with AgNW as the thermally conductive bridges. *Compos. Sci. Technol.* **196**, 108242 (2020).
65. Y. S. Ju, K. Kurabayashi, K. E. Goodson, Thermal characterization of anisotropic thin dielectric films using harmonic joule heating. *Thin Solid Films* **339**, 160-164 (1999).
66. E. Pop, The role of electrical and thermal contact resistance for joule breakdown of single-wall carbon nanotubes. *Nanotechnology* **19**, 295202 (2008).
67. Z.-Y. Ong, E. Pop, Molecular dynamics simulation of thermal boundary conductance between carbon nanotubes and SiO₂. *Phys. Rev. B* **81**, 155408 (2010).
68. E. Pop, D. Mann, J. Reifenberg, K. Goodson, H. Dai, in *IEEE International Electron Devices Meeting, 2005. IEDM Technical Digest.* (IEEE, 2005), pp. 4 pp.-256.
69. K. Miyazaki, K. Kuriyama, T. Yabuki, Printable thermoelectric device. *J. Phys. Conf. Ser.* **1407**, 012057 (2019).
70. A. Cappella *et al.*, High temperature thermal conductivity of amorphous Al₂O₃ thin films grown by low temperature ald. *Adv. Eng. Mater.* **15**, 1046-1050 (2013).
71. C. Monachon, L. Weber, C. Dames, Thermal boundary conductance: A materials science perspective. *Annu. Rev. Mater. Res.* **46**, 433-463 (2016).
72. P. E. Hopkins, R. N. Salaway, R. J. Stevens, P. M. Norris, Temperature-dependent thermal boundary conductance at Al/Al₂O₃ and Pt/ Al₂O₃ interfaces. *Int. J. Thermophys.* **28**, 947-957 (2007).

Acknowledgements

Funding: This work was supported by the National Key R&D Program of China (Grant No. 2022YFB4401603 and 2021YFA1202904) and Peking Nanofab. H.S. and E.P. acknowledge partial support from SUPREME, one of the seven JUMP 2.0 centers sponsored by Semiconductor Research Corporation (SRC) and DARPA.

Author contributions: Y.H. and L.-M.P. proposed and supervised the project. F.X. and T.X designed flexible RF devices and conducted device fabrication. H.S. performed the finite-element electro-thermal modeling. F.X., T.X., Q.H., T.B., and G.L. performed the S-parameter measurements. L.G., W.W. and C.M. performed the flexibility tests. L.G., R.H., and Y.C. prepared flexible substrates. F.X., T.X, H.S., E.P., L.-M.P., and Y.H. analyzed the data and co-wrote the manuscript. All the authors discussed the results and revised the manuscript.

Competing interests: The authors declare no competing interests.

Data availability: The data that support the findings of this study are available from the corresponding author upon reasonable request.

Supplementary Materials

Materials and Methods

Supplementary Text

Figs. S1 to S10

Tables S1 to S3

References (49-72)

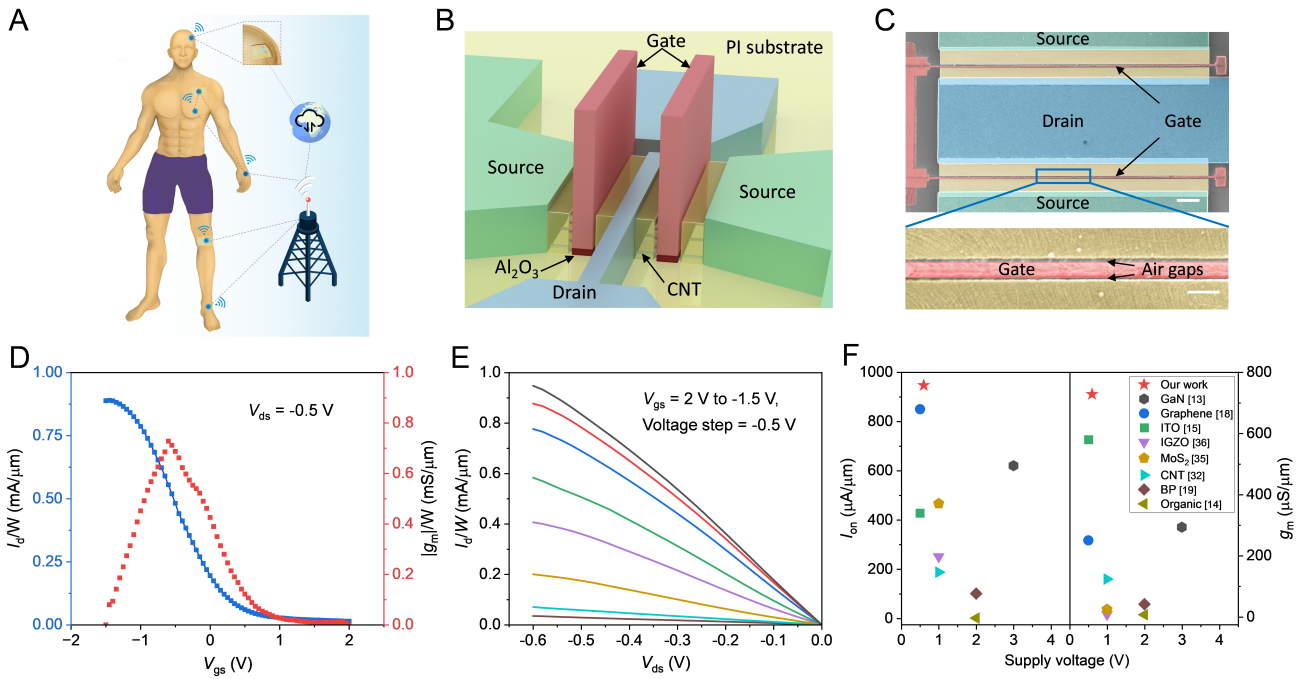


Fig. 1 Structure and DC characteristics of flexible CNT-based RF transistors. (A) Conceptual illustration of seamlessly integrable terminals for human-centric communications in 6G technology. (B) Schematic of the structure of a flexible RF transistor based on aligned CNT arrays. (C) Top: SEM image of a two-fingered flexible RF transistor with $L_g = 75$ nm and $L_{ch} = 120$ nm. Scale bar: 1 μ m. Bottom: Zoomed-in SEM image of the channel area. Scale bar: 300 nm. (D) Transfer characteristics (blue curve) and transconductance (red curve) for a flexible RF transistor with $L_g = 75$ nm and $L_{ch} = 120$ nm. (E) Output characteristics of the same transistor of (C). (F) Comparison of I_{on} and g_m versus supply voltages between our flexible RF transistors and previously reported flexible RF transistors based on various materials, including GaN (13), indium tin oxide (ITO) (15), indium gallium zinc oxide (IGZO) (36), MoS₂ (35), CNT (32), black phosphorus (BP) (19), graphene (18), and organic materials (14).

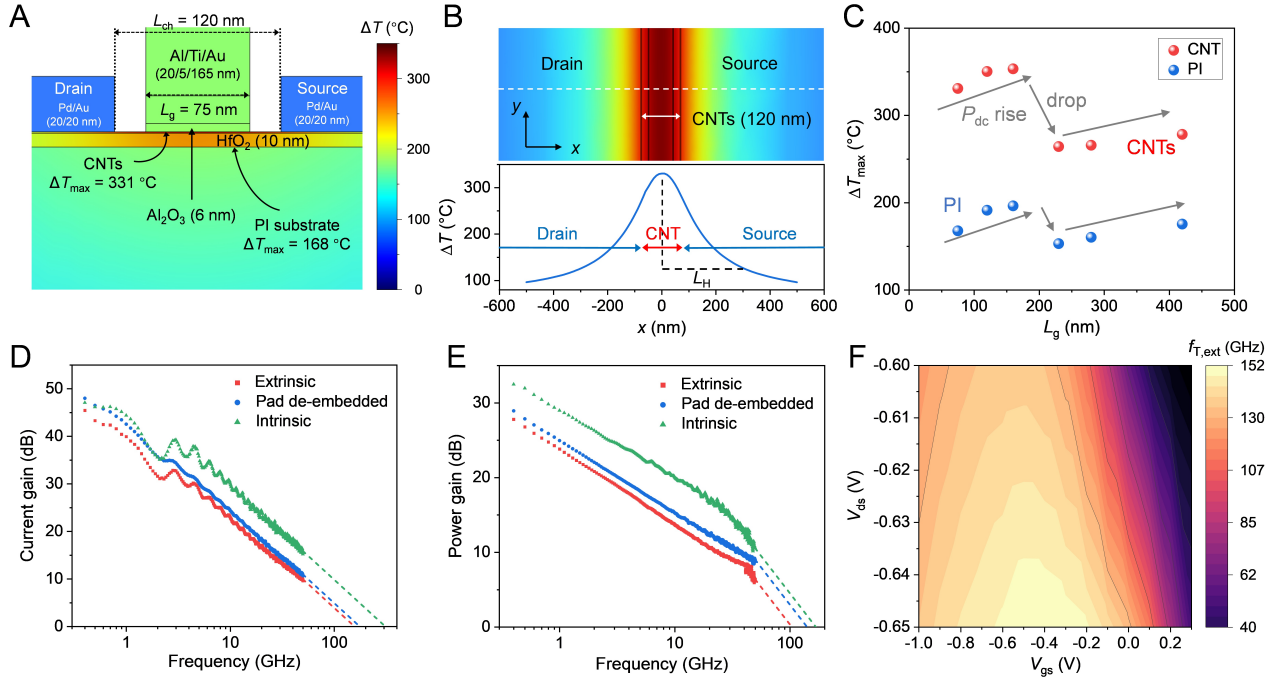


Fig. 2 Electro-thermal co-design and performance of flexible CNT-based RF transistors. (A) Heat map showing the temperature rise (ΔT) of a flexible RF transistor with $L_g = 75$ nm at a power of 1.99 mW. The power was measured under bias conditions when the maximum f_T was reached. (B) Top: Zoomed-in x - y cross-section view of the device in (A) around the channel area. Bottom: ΔT profile along the CNT channel direction (dashed line in the top figure), showing the temperature decay over a characteristic thermal length $L_H \approx 300$ nm. (C) Maximum ΔT of the CNT channel and the PI substrate with different L_g . The input power varies here for different L_g , as shown in fig. S4C. (D) Extrinsic, pad de-embedded, and intrinsic current gains versus frequency for the champion flexible RF transistor with $L_g = 75$ nm. (E) Extrinsic, pad de-embedded, and intrinsic power gains versus frequency for the champion flexible RF transistor with $L_g = 160$ nm. The slope of the extension line is -20 dB dec^{-1} . (F) $f_{T,\text{ext}}$ as a function of bias conditions, V_{gs} and V_{ds} .

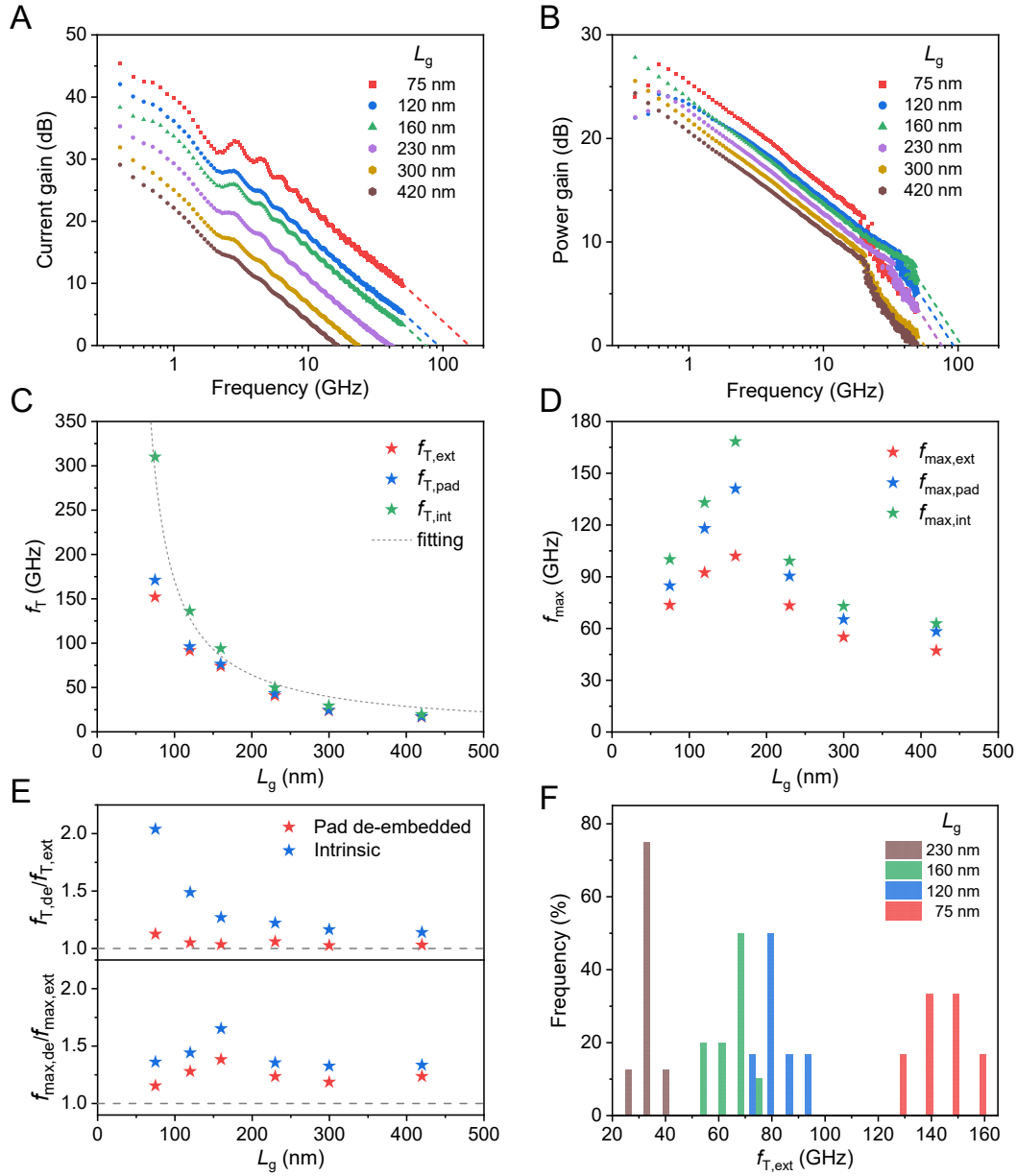


Fig. 3 Performance of flexible RF transistors with different L_g . (A and B) Extrinsic current gain (A) and extrinsic power gain (B) versus frequency for representative flexible RF transistors with different L_g . The slope of the extension line is -20 dB dec^{-1} . (C) Changes in the extrinsic, pad de-embedded, and intrinsic f_T with L_g . The $f_{T,int}$ is fitted with an inversely proportional function with L_g ($f_{T,int} \propto 1/L_g$, dashed curve). (D) Changes in the extrinsic, pad de-embedded, and intrinsic f_{max} with L_g . (E) Pad and intrinsic de-embedding ratios for flexible RF transistors with different L_g , with dashed lines representing the de-embedding ratio of 1. (F) Statistical distributions of $f_{T,ext}$ for flexible RF transistors with different L_g .

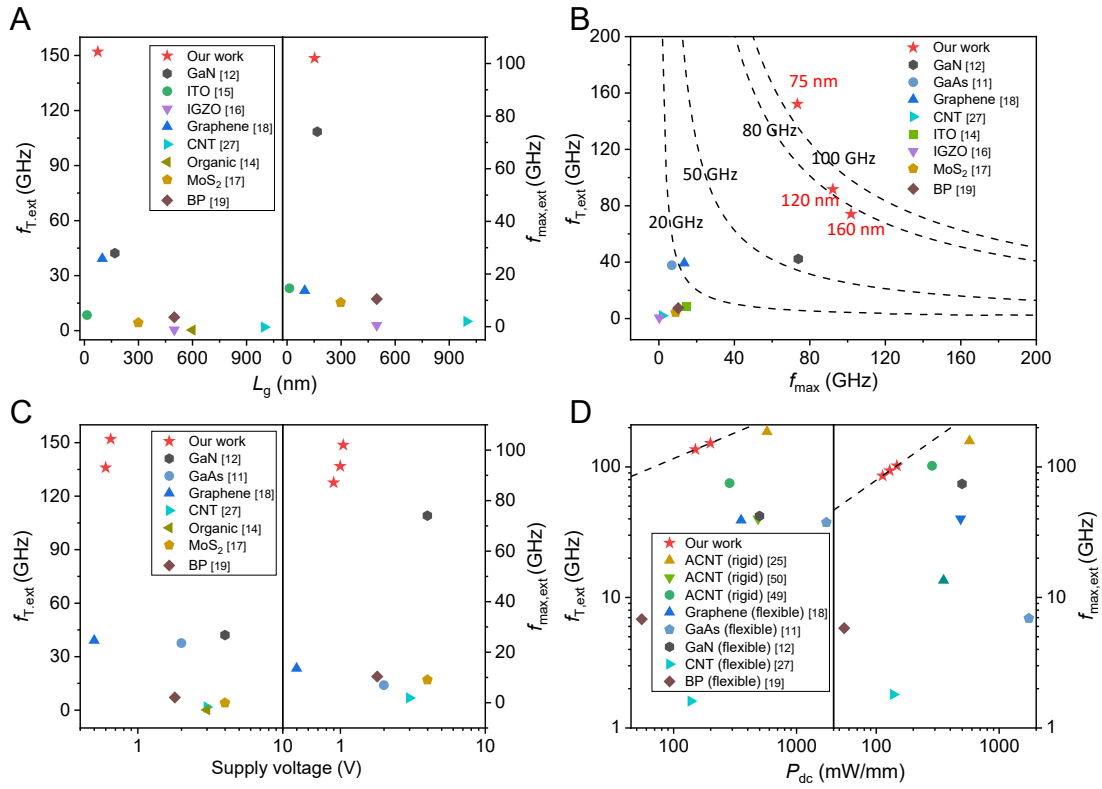


Fig. 4 Benchmarking of performance and power consumption. (A) Comparison of $f_{T,ext}$ (left) and $f_{max,ext}$ (right) versus L_g between our work and other flexible RF transistors based on various materials. (B) Comparison of $f_{T,ext}$ versus $f_{max,ext}$ between our work and other flexible RF transistors. The three data points from our work correspond to flexible RF transistors with $L_g = 75$ nm, 120 nm, and 160 nm. Dashed curves represent contour lines when the geometric mean, $(f_{T,ext} \times f_{max,ext})^{1/2}$, is 20 GHz, 50 GHz, 80 GHz, and 100 GHz. (C) Comparison of $f_{T,ext}$ (left) and $f_{max,ext}$ (right) versus the supply voltage between our work and other flexible RF transistors. (D) Comparison of $f_{T,ext}$ (left) and $f_{max,ext}$ (right) versus P_{dc} among flexible RF transistors based on different materials and CNT-based RF transistors on rigid substrates.

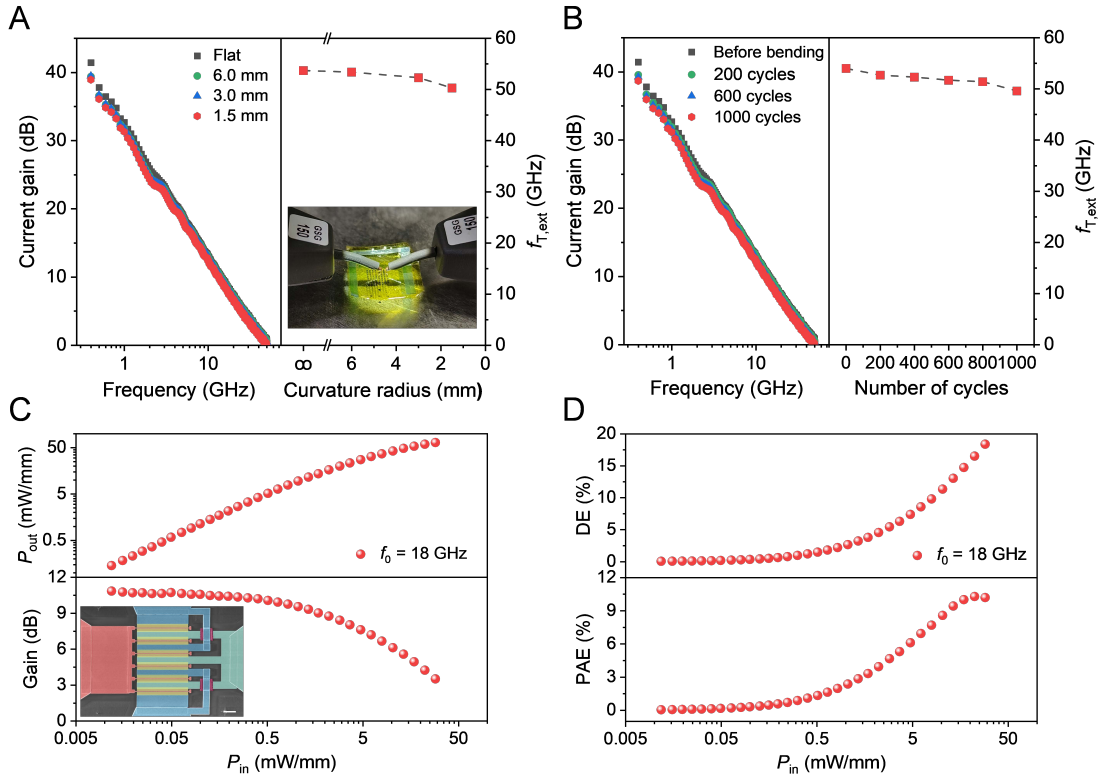


Fig. 5 Flexibility test of flexible RF transistors and performance of flexible power amplifiers. (A) Current gain of a typical flexible RF transistor with $L_g = 200$ nm under different bending radii of curvature (left) and the relationship between $f_{T,ext}$ and the curvature radius (right). Inset: Photograph showing electric characterization of the flexible RF transistors after being released from bending. (B) Current gain of a typical flexible RF transistor after multiple bending cycles with a curvature radius of 3 mm (left) and the relationship between $f_{T,ext}$ and number of bending cycles (right). (C) The output power (P_{out} , top) and power gain (bottom) versus input power (P_{in}) for a flexible RF power amplifier with $L_g = 160$ nm operating at a f_0 of 18 GHz. Bias conditions are $V_{gs} = -0.8$ V and $V_{ds} = -1.0$ V. The source and load impedances are 50Ω and $47.32 + 46.67j \Omega$, respectively. Inset: SEM image of the flexible RF power amplifier. Scale bar: $3 \mu\text{m}$. (D) The drain efficiency (DE, top) and the power-added efficiency (PAE, bottom) versus P_{in} for a flexible RF power amplifier operating at a f_0 of 18 GHz.

Supplementary Materials for

Flexible radio-frequency transistors exceeding 100 GHz

Fan Xia^{1†}, Tian Xia^{1,3†}, Haotian Su^{2†}, Lanyue Gan¹, Qianlan Hu¹, Wanyi Wang¹, Ruyi Huang^{1,3}, Tianshun Bai¹, Yufan Chen¹, Chao Ma¹, Guanhua Long¹, Shan X. Wang², Eric Pop^{2*},
Lian-Mao Peng^{1,3*}, Youfan Hu^{1,3*}

Corresponding author: epop@stanford.edu, lpeng@pku.edu.cn, youfanhu@pku.edu.cn

The PDF file includes:

Materials and Methods
Supplementary Text
Figs. S1 to S10
Tables S1 to S3
References

Materials and Methods

Fabrication of the flexible substrates

First, the PI solution (593052, Sigma-Aldrich) was spin-coated onto a rigid temporary supporting substrate (silicon wafer) at a speed of 5000 rpm. Then, a step baking process was carried out to remove the solvent and complete the polyimide imidization process. The optimized baking protocol included three steps: 100 °C for 10 min, 250 °C for 60 min, and 375 °C for 60 min. Finally, a 10-nm-thick HfO₂ layer was deposited on the cured PI surface using atomic layer deposition (ALD) (TFS 200, Beneq Oy.) at 90 °C. This HfO₂ layer enhanced the adhesive strength between the metal layer and the flexible substrate and improved heat dissipation.

Transfer of the aligned CNT arrays to the flexible substrate

Poly(methyl methacrylate) (PMMA) was spin-coated onto the aligned CNT arrays on the silicon wafer. The sample was then immersed in hydrofluoric acid for 7 days to etch the surface SiO₂ layer and detach the aligned CNT arrays from the wafer. Once separated, the CNT film was cleaned by deionized water and transferred onto the target flexible substrate. The sample was then baked at 60 °C for 10 min to stabilize the transfer, followed by soaking in acetone for 2 h to dissolve the PMMA film.

Fabrication of flexible RF transistors and power amplifiers

First, Ti/Au bilayer films (10/80 nm) were patterned to form alignment markers and interconnecting wires by electron beam lithography (EBL) (Voyager, Raith GmbH), electron beam evaporation (EBE) (DE 400, DE Technology), and a standard lift-off process. Reactive ion etching (Minilock, Trion) was then performed to etch away the unwanted CNTs outside the channel regions defined by EBL. Following this, Pd/Au films (20/20 nm) were deposited to form the source and drain electrodes. A 2.5 nm Al layer was subsequently deposited and oxidized in air to form Al₂O₃ as the gate dielectrics. Al/Ti/Au films (20/5/165 nm) were deposited next to form the gate electrodes. For interconnecting wires and RF input and output pads, Ti/Au films (20/400 nm) were deposited. In the case of power amplifiers with 6 fingers, overexposed PMMA (50k, 12%) bridges were utilized as jumpers between the lower and upper interconnecting wires. Finally, the complete flexible electronic chip was exfoliated from the temporary supporting substrate using a capillary-assisted electrochemical delamination method, as described below.

Capillary-assisted electrochemical delamination

A NaCl electrolyte solution (1 mol L⁻¹) was first prepared. After trimming off the fringes of the PI layer to expose the surface of the silicon wafer, the sample was fixed at 45° by clamping equipment, with the electronic devices facing upward. The lower edge of the silicon wafer was then inserted in the NaCl solution. A positive potential of 20 V was applied to the silicon wafer, while the NaCl solution was grounded at 0V. This setup initiated the anodic reaction of $\text{Si} - 8\text{e}^- + 8\text{OH}^- \rightarrow \text{H}_2\text{SiO}_3\downarrow + 3\text{H}_2\text{O} + 2\text{O}_2\uparrow$, generating gaps between the PI layer and silicon wafer. The resulting capillary force allowed the NaCl solution to climb upwards, facilitating the delamination of the PI along the inclined silicon wafer.

Measurement of the flexible RF transistors and power amplifiers

The flexible electronic chip was placed flat on a supporting quartz substrate for probe testing. The setup for S-parameter measurements included a probe station (Cascade Summit 200), ground-signal-ground (GSG) probes, coaxial cables, a semiconductor analyzer (Agilent B1500) and a

vector network analyzer (Keysight N5247B). The GSG probes and coaxial cables were first calibrated using the standard off-wafer short–open–load–through (SOLT) procedure. The semiconductor analyzer provided the DC bias, while the vector network analyzer supplied the RF signal. For power amplifier measurements, a pair of impedance tuners (FOCUS L4030) were used for impedance matching.

Supplementary Text

Finite-Element Electro-Thermal Modeling

We estimate the temperature rise (ΔT , above room temperature) in our CNT FETs using finite-element electro-thermal modeling (35). Devices with varying channel lengths and operating characteristics, as listed in table S2 below, were modeled to estimate their peak ΔT . These specific devices and operating conditions were simulated at the power levels that devices experience during our RF measurements, as discussed in the main text. We conducted the steady-state simulations of CNT transistors with dimensions shown in fig. S4A. The bottom of the 2 μm thick PI substrate is taken as the thermal ground (fixed at 20 $^{\circ}\text{C}$), because it was attached to a metal chuck during our RF measurement. (We tested the simulation with an interfacial thermal conductance between the PI and metal chuck (35, 49-51), $h_c \approx 10^5 \text{ Wm}^{-2}\text{K}^{-1}$, but found this has little impact on the simulated peak ΔT .)

The thermal conductivity (TC) of the materials and thermal boundary conductance (TBC) at material interfaces used in our simulations are given in table S3. Significant variations in CNT TC have been reported in the literature (52-54). For example, the TC of CNTs depends on factors such as their quality, diameter, length, density, and the substrate on which they are sitting. For our dense (~ 150 CNTs/ μm) aligned CNTs on HfO_2 , the TC of such arrays remains largely unknown. Moreover, predicting the TC of CNTs using the Wiedemann-Franz law (55, 56) is challenging, as phonons, rather than electrons, dominate heat conduction along CNTs and their contacts across all temperatures of practical interest (40). Consequently, we used the TC values from the theoretical work by Volkov *et al.* (57) as a guideline when estimating the TC of our CNT arrays.

To estimate the peak ΔT in our devices, we also need to determine the electrical power distribution across the device. Despite the shortest channel length being 120 nm, our devices are not in the quasi-ballistic regime because the average total resistance per CNT is $\approx 78.4 \text{ k}\Omega$ ($\sim 56.4 \text{ }\Omega$ device total resistance extracted from Fig. 1E and for $\sim 1,500$ CNTs in parallel), significantly higher than the quantum ballistic transport limit of single CNT, with $\sim 6.5 \text{ k}\Omega$ resistance (58). Thus, we model the CNT arrays with uniform sheet resistance across their length. Pd metal is used to form high-quality ohmic contacts at the source and drain, to minimize contact resistance (31, 58-60). In fig. S4B, the simulated top view of the ΔT distribution for a CNT FET with $L_{\text{ch}} = 120 \text{ nm}$ shows minimal temperature rise of the big metal Source/Drain and Gate pads.

To understand the temperature profile in our devices, we estimate the thermal healing length (i.e., the characteristic temperature decay length) along the CNT channel, written generally as (61):

$$L_{\text{H}} = \sqrt{\frac{k_{\text{film}} d_{\text{film}} d_{\text{substrate}}}{k_{\text{substrate}}}},$$

where k_{film} and d_{film} are the thermal conductivity and thickness of the heater element (here, the CNTs), while $k_{\text{substrate}}$ and $d_{\text{substrate}}$ are the thermal conductivity and thickness of the substrate under the heater. To make this more specific to the CNT devices, we can rewrite their L_H as:

$$L_H = \sqrt{k_{\text{CNT,In-plane}} d_{\text{CNT}} R_{\text{th}}},$$

where R_{th} is the thermal resistance between CNT and heat sink at the bottom of the PI:

$$R_{\text{th}} = \frac{1}{G_{\text{CNT-PI}}} + R_{\text{PI}}.$$

Here R_{PI} is the thermal resistance of the PI substrate, accounting for the shape factor of a circular disk heater on a semi-infinite substrate (45, 62), which has also been found as a good approximation for a rectangular heater (i.e., the shape of the transistor channel):

$$R_{\text{PI}} \approx \frac{WL}{2k_{\text{PI,eff}}},$$

where $k_{\text{PI,eff}} \approx (k_{\text{PI,cross-plane}} \times k_{\text{PI,In-plane}})^{1/2}$, and $G_{\text{CNT-PI}}$ is the total thermal conductance between the channel of CNTs and PI substrate, including the TBC at CNT-HfO₂ and HfO₂-PI interfaces, and the thermal conductance of the HfO₂ insulator [see fig. S4A]:

$$G_{\text{CNT-PI}} = \left(\frac{1}{\text{TBC}_{\text{CNT-HfO}_2}} + \frac{1}{\text{TBC}_{\text{HfO}_2\text{-PI}}} + \frac{d_{\text{HfO}_2}}{k_{\text{HfO}_2}} \right)^{-1}.$$

With TC and TBC values in table S3, using L_{ch} of 120 nm, we estimate $L_H \approx 283$ nm along the CNT channel. This closely matches our simulation results, which show $L_H \approx 300$ nm, as shown in Fig. 2B of the main text.

We also conducted the sensitivity analysis of device temperature with respect to various material properties. Increasing (i.e., doubling) the in-plane TC of CNTs to 100 Wm⁻¹K⁻¹ resulted in a ~20% drop in the maximum CNT channel temperature. Additionally, to address uncertainties in TBCs at various material interfaces, we adopted conservative assumptions using lower-bound estimates (as detailed in table S3) to model the worst-case scenario. Our approach thus provides an upper-bound estimate for the peak device temperature.

De-embedding Procedure of Flexible RF Transistors

A standard open-short de-embedding method was employed for pad and intrinsic de-embedding. The process is outlined as follows:

- (1) Measure the S-parameters of the device under test (DUT), open structure, and short structure.
- (2) Convert the measured S-parameters (S_{DUT} , S_{Open} , S_{Short}) to Y-parameters (Y_{DUT} , Y_{Open} , Y_{Short}).
- (3) Calculate the de-embedded Y-parameters $Y_{\text{de-embed}}$ using the following equation:

$$\frac{1}{Y_{\text{de-embed}}} = \frac{1}{Y_{\text{DUT}} - Y_{\text{Open}}} - \frac{1}{Y_{\text{Short}} - Y_{\text{Open}}}.$$

- (4) Convert the de-embedded Y-parameters $Y_{\text{de-embed}}$ back to de-embedded S-parameters $S_{\text{de-}}$

embed.

(5) Calculate the de-embedded f_T and f_{\max} using the de-embedded S-parameters $S_{\text{de-embed}}$.

Two types of de-embedding open and short structures were used: pad de-embedding structures and intrinsic de-embedding structures. The pad de-embedding structures, shown in fig. S6, A and B (with zoomed-in views in fig. S6, C and D, respectively), consist solely of the pads of the flexible RF transistor. In contrast, the intrinsic de-embedding structures, illustrated in figs. S6, E and F, include the connection wires and electrodes of the flexible RF transistor. The S-parameters of the pad de-embedding short and open structure are shown in fig. S9 as Smith charts. The S_{11} and S_{22} of the open structure are located near the infinite point of impedance, indicating minimal parasitic effects from the substrate and the measurement system.

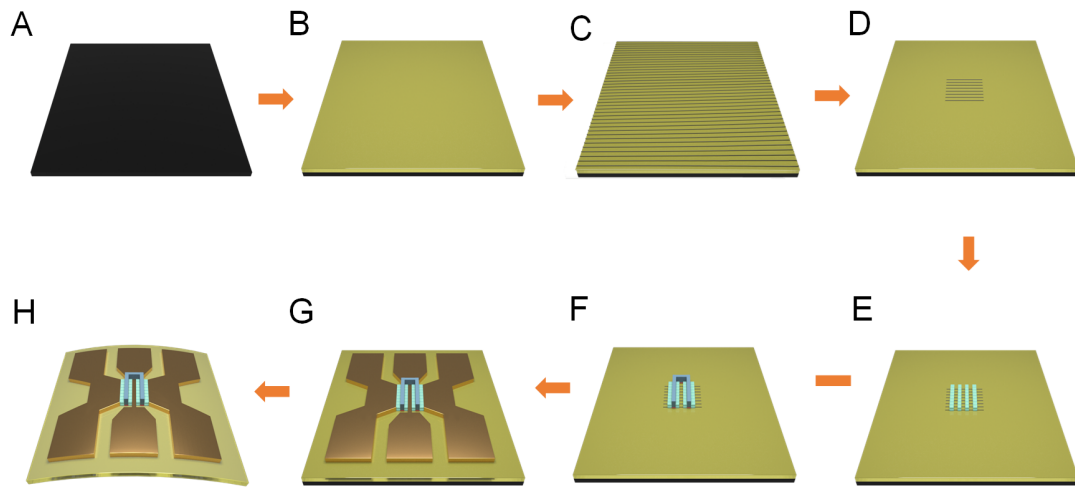


Fig. S1. Fabrication process of flexible RF transistors. (A) Preparation of the rigid temporary supporting substrate (silicon wafer). (B) Preparation of the flexible substrate (PI) with low dielectric loss and low surface roughness. (C) Transfer of the aligned CNT arrays. (D) Etching of the unwanted CNTs. (E) Deposition of source and drain electrodes. (F) Deposition of gate dielectrics and gate electrodes. (G) Deposition of RF input and output pads. (H) Exfoliation of the flexible electronic chip from the temporary supporting substrate.

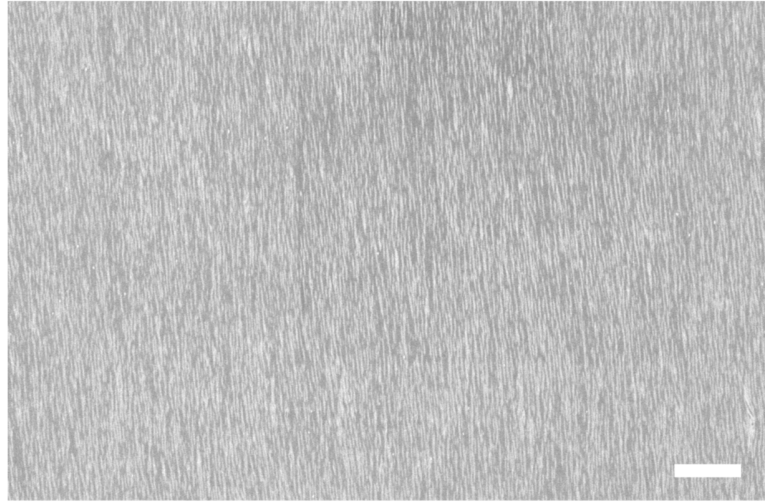


Fig. S2. SEM image of the CNT material. SEM image of aligned CNT arrays in the channel region of the flexible RF transistor. Scale bar: 1 μm .

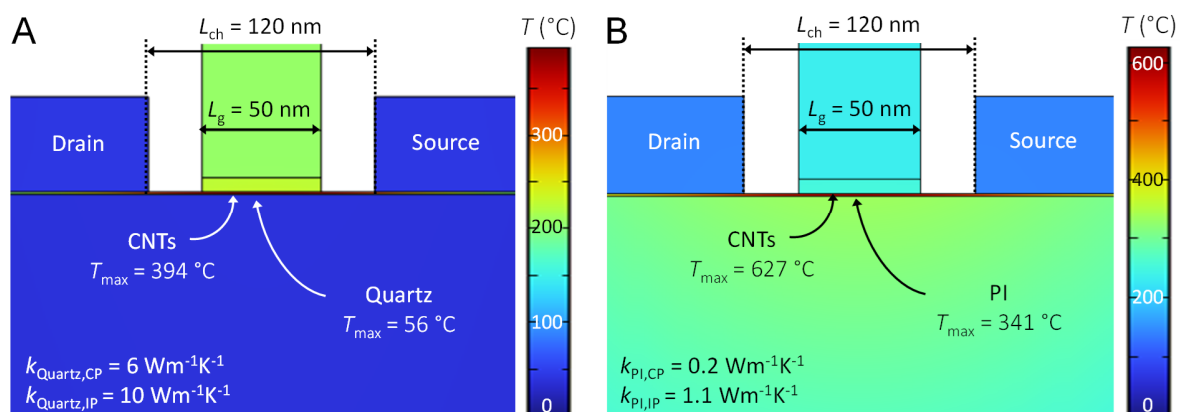


Fig. S3. Finite-element electro-thermal simulation of an electrically optimized CNT-based RF transistor. (A and B) Heat map showing the temperature distribution of a state-of-the-art RF transistor on the rigid substrate (crystal quartz) (A) and the flexible substrate (PI) (B), with the same power input of 3.36 mW (25).

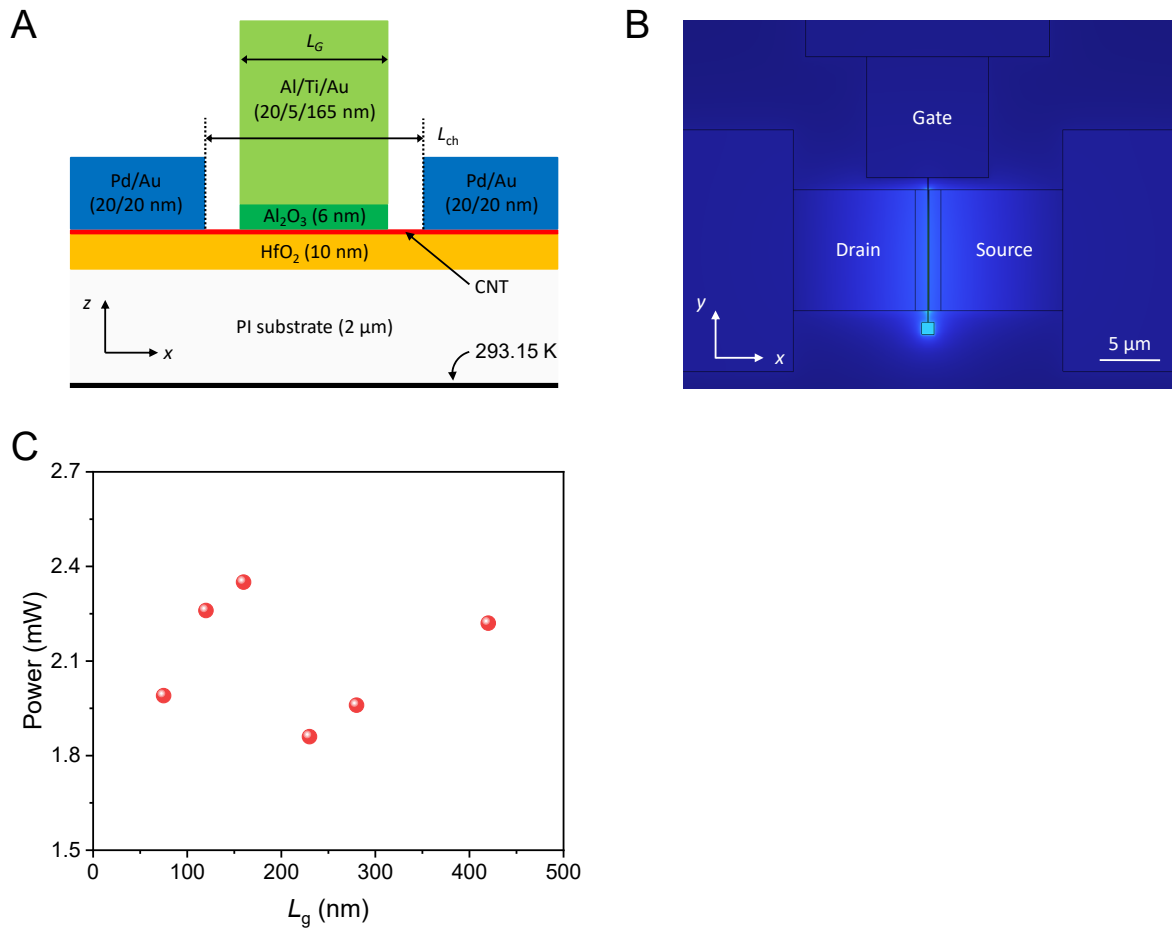


Fig. S4. Finite-element electro-thermal simulation of flexible CNT-based RF transistors. (A) Cross-section schematic of the CNT transistor, showing the dimensions of each segment (not drawn to scale). The bottom of the PI substrate is set to room temperature, 20 °C. (B) Simulated top view temperature map of the CNT transistor with $L_{ch} = 120$ nm, showing negligible temperature rise at the electrode pads. A zoomed-in temperature profile is provided in Fig. 2, A and B of the main text. (C) The power of the flexible RF transistor for different L_g .

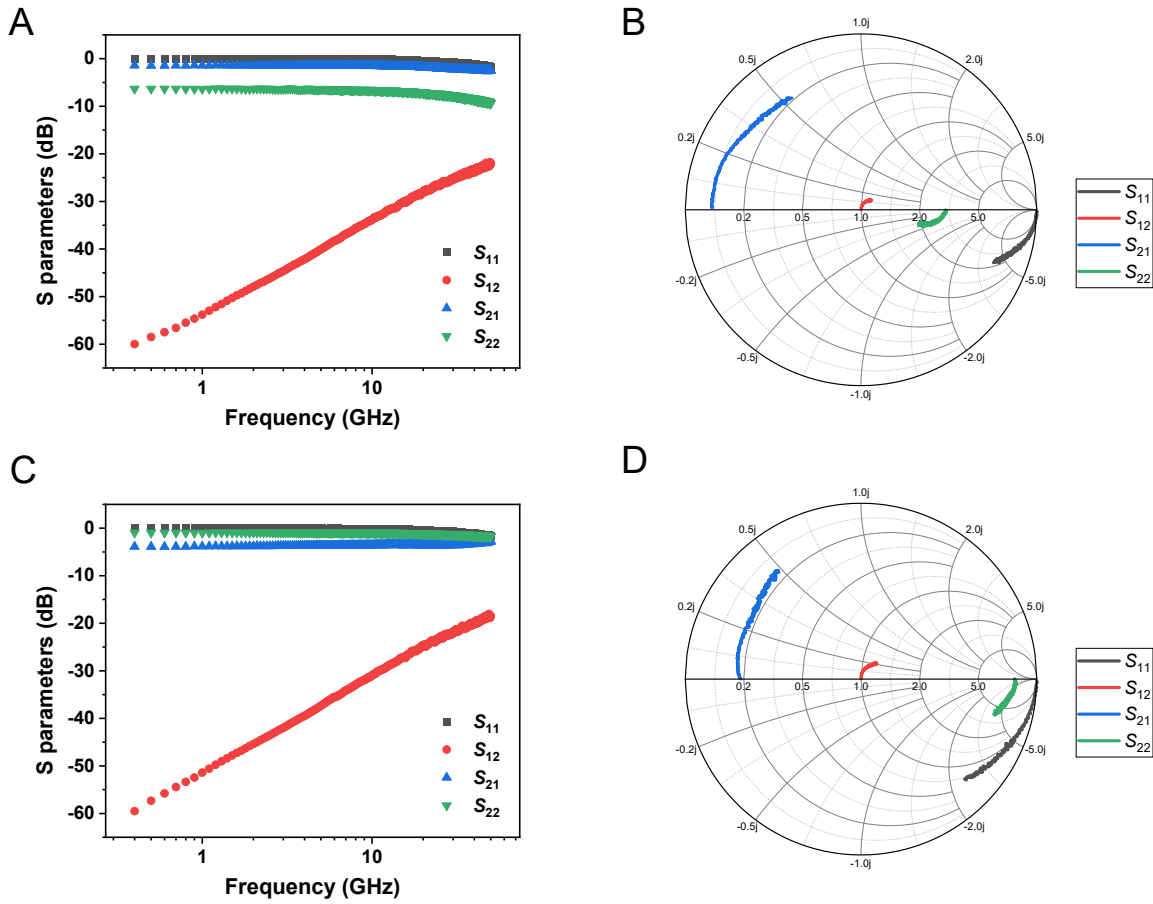


Fig. S5. S-parameters of flexible CNT-based RF transistors. (A) Measured S-parameters for the flexible RF transistor with $L_g = 75$ nm as a function of input signal frequency. **(B)** Smith chart representation of the S-parameters measured in (A). **(C)** Measured modulus of the S-parameters for the flexible RF transistor with $L_g = 160$ nm as a function of input signal frequency. **(D)** Smith chart representation of the S-parameters measured in (C).

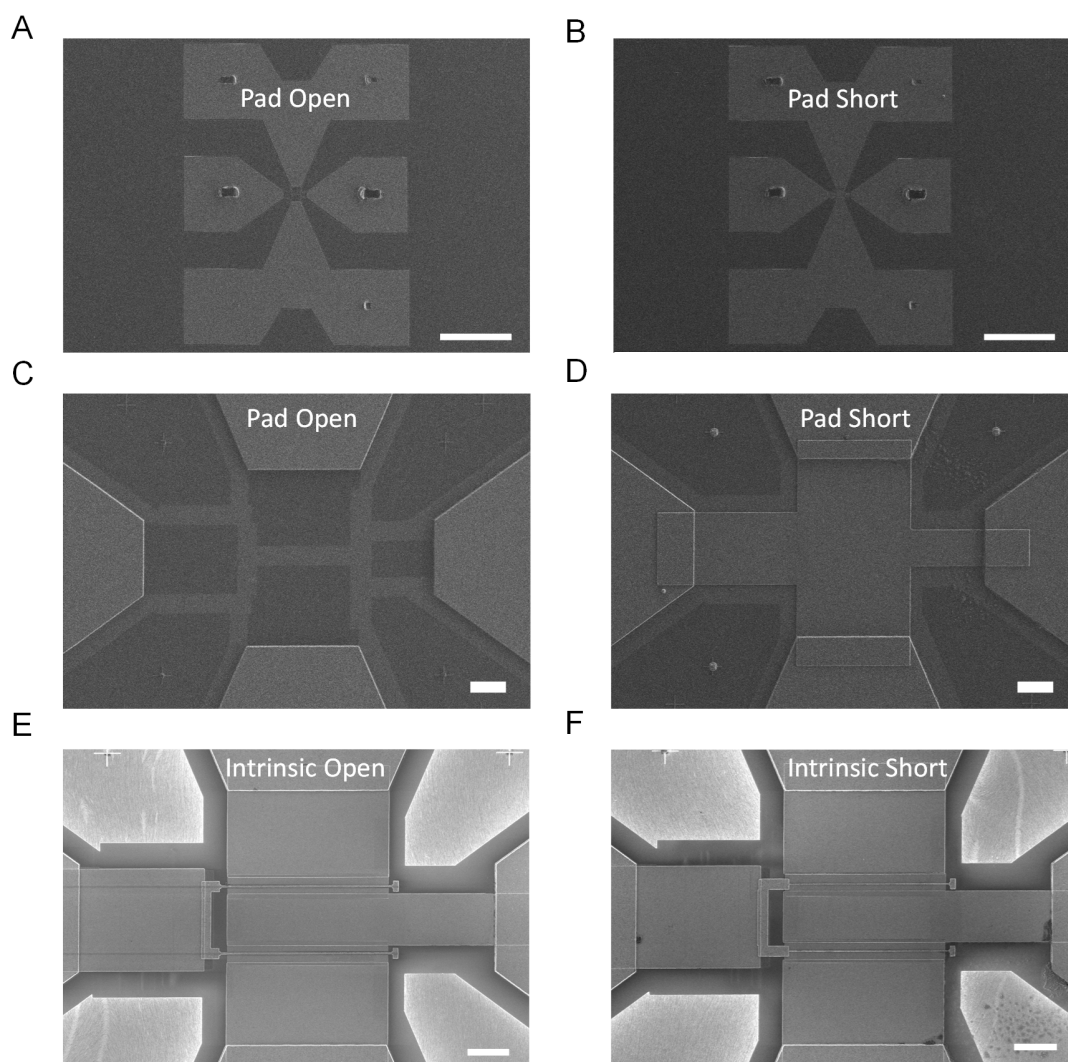


Fig. S6. SEM images of de-embedding structures. (A and B) SEM images of the pad de-embedding open (A) and short structures (B). Scale bar: 100 μm . (C and D) Zoomed-in SEM images of the pad de-embedding open (C) and short structures (D). Scale bar: 4 μm . (E and F) Intrinsic de-embedding open (E) and short structures (F). Scale bar: 3 μm .

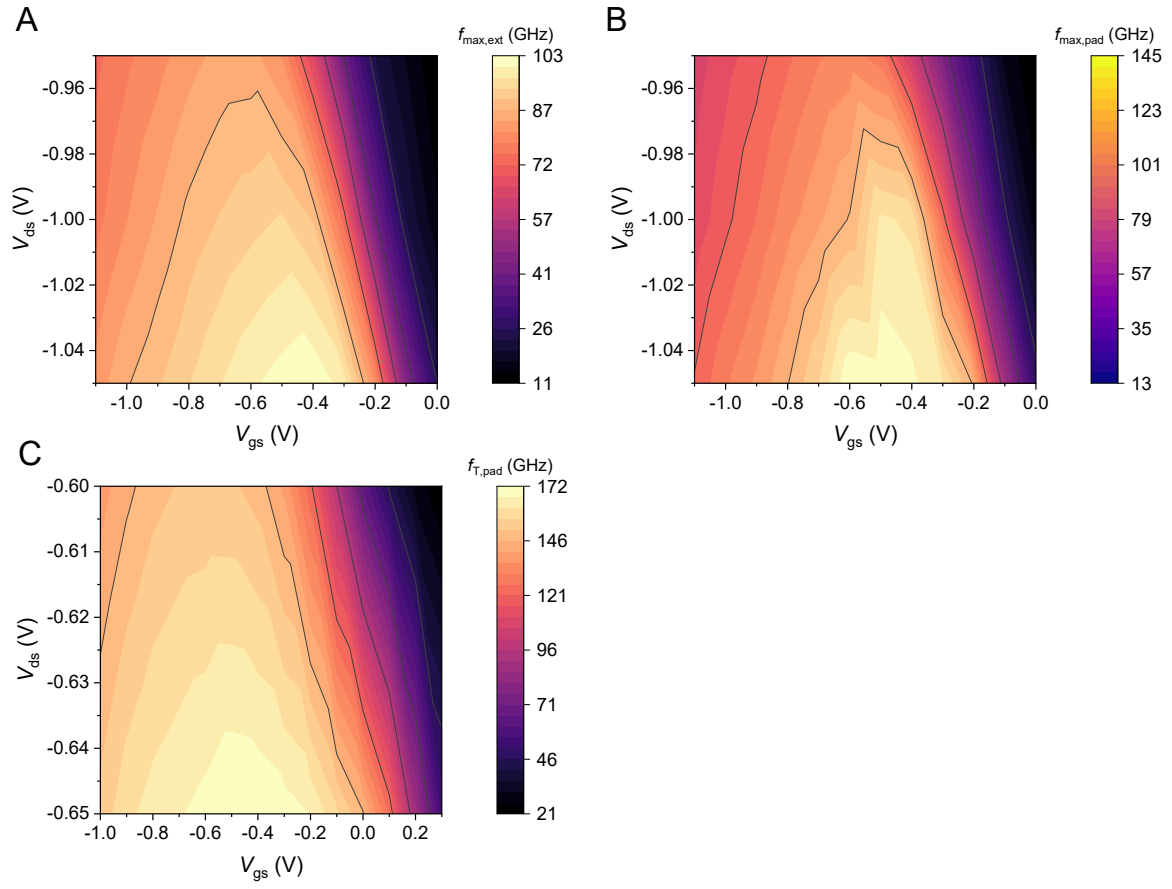


Fig. S7. Bias conditions to achieve the highest $f_{\max, \text{ext}}$, $f_{T, \text{pad}}$, $f_{\max, \text{pad}}$. (A and B), Bias conditions (V_{gs} and V_{ds}) of $f_{\max, \text{ext}}$ (A) and $f_{\max, \text{pad}}$ (B) for the flexible RF transistor with $L_g = 160$ nm. (C) Bias conditions (V_{gs} and V_{ds}) of $f_{T, \text{pad}}$ for the flexible RF transistor with $L_g = 75$ nm.

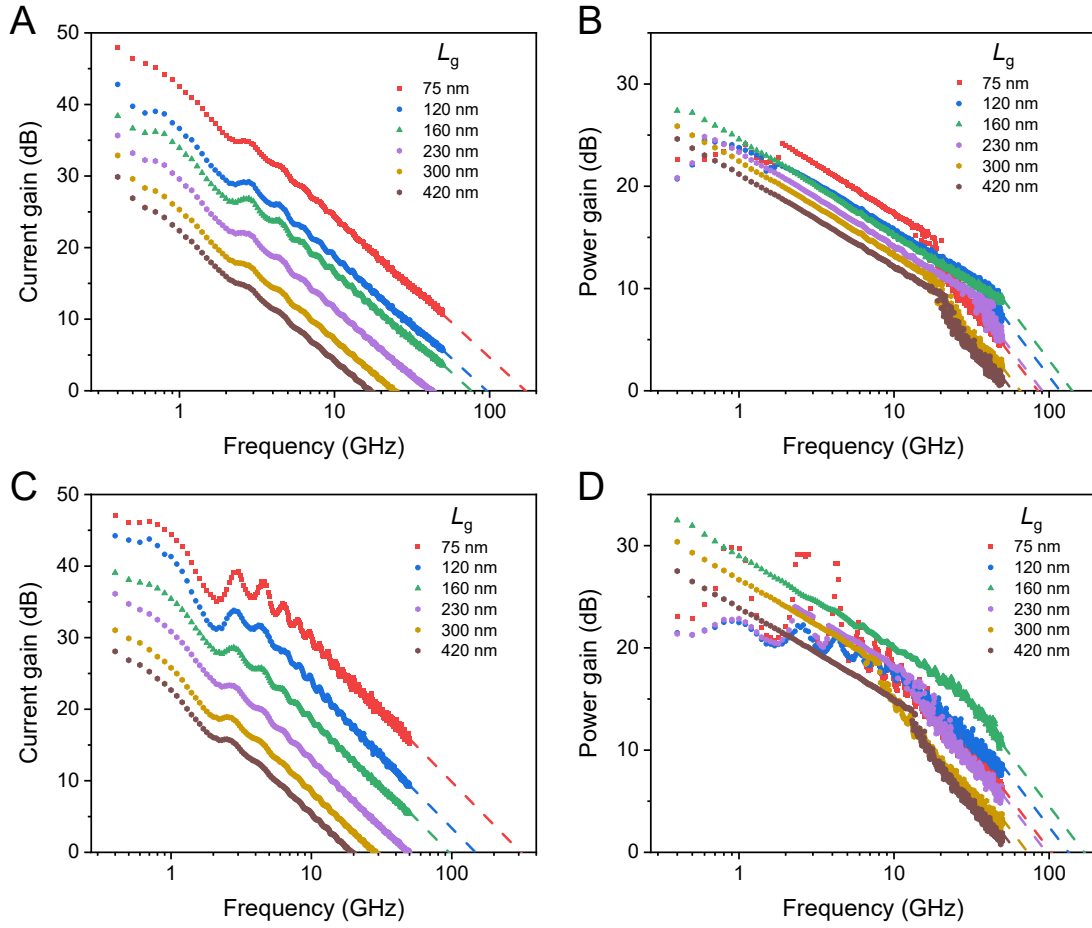


Fig. S8. Pad de-embedded and intrinsic performance of flexible RF transistors with different L_g . (A and B), Pad de-embedded current gains (A) and power gains (B) of flexible RF transistors based on aligned CNTs with different L_g values as a function of input signal frequency from the S-parameter measurements. (C and D) Intrinsic de-embedded current gains (C) and power gains (D) of flexible RF transistors with different L_g values. The input power for the small signal is -10 dBm. The upper-frequency limit of the measurement instrument is 50 GHz, and the lines beyond 50 GHz were extrapolated with a slope of -20 dB per decade.

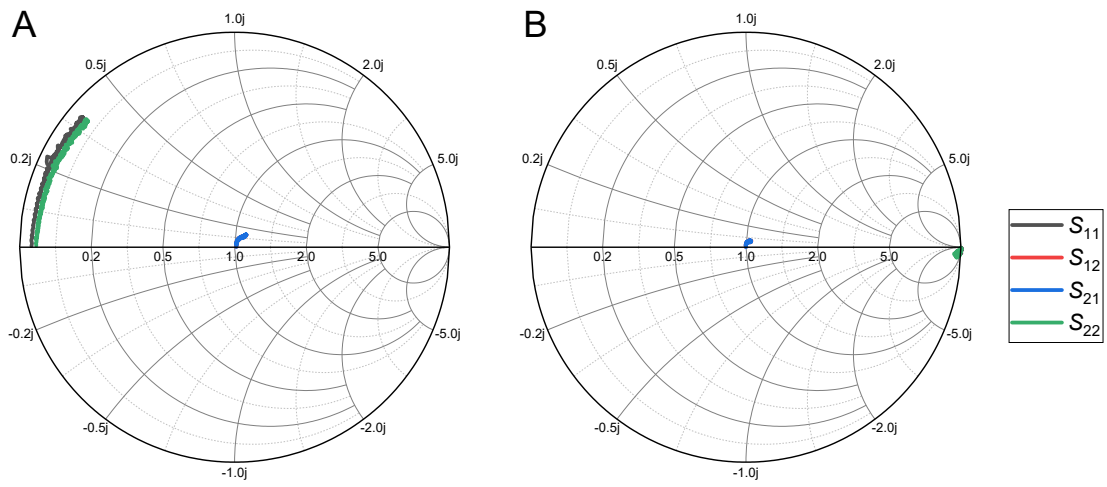


Fig. S9. S-parameters of pad de-embedding structures. (A and B) S-parameters of the pad de-embedding short (A) and open structure (B) plotted in Smith charts.

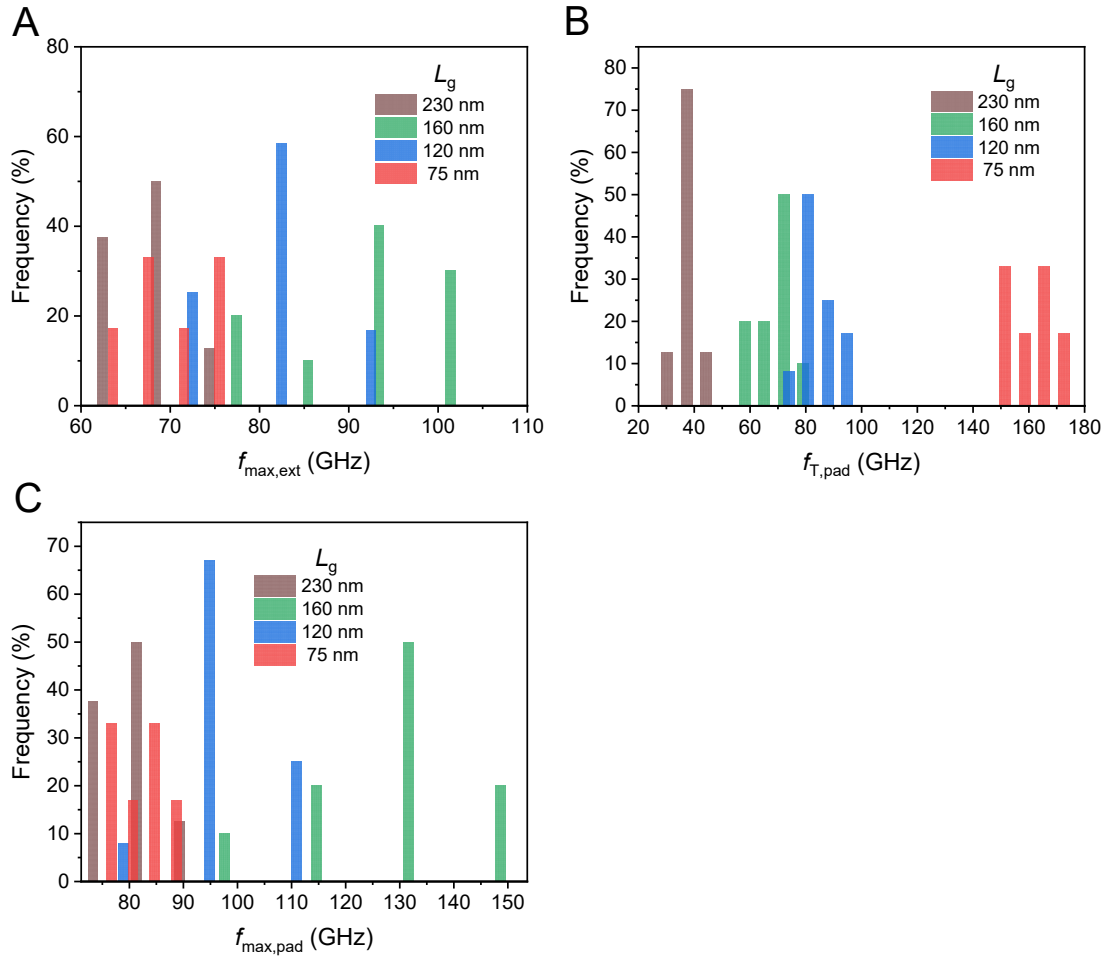


Fig. S10. Statistical distributions of the $f_{\max, \text{ext}}$, $f_{T, \text{pad}}$ and $f_{\max, \text{pad}}$. (A, B and C) Statistical distributions of $f_{\max, \text{ext}}$ (A), $f_{T, \text{pad}}$ (B) and $f_{\max, \text{pad}}$ (C) for 12 flexible RF transistors, each with the L_g of 120 nm, 60 nm and 230 nm. The average values and standard deviations summarized in table S1, highlighting the excellent uniformity of the devices.

Table S1. Average values and standard deviations of the extrinsic and pad de-embedded f_T and f_{max} .

L_g (nm)	$f_{T,ext}$ (GHz)	$f_{max,ext}$ (GHz)	$f_{T,pad}$ (GHz)	$f_{max,pad}$ (GHz)
75	141.17±9.20	68.33±4.13	158.67±7.92	78.50±4.59
120	80.17±5.84	79.93±7.44	83.67±6.34	97.36±11.46
160	66.96±5.95	92.34±9.23	69.05±6.29	127.24±17.09
230	37.11±2.48	67.42±3.98	39.14±2.47	81.58±5.83

Table S2. Device characteristics used in the finite-element electro-thermal simulations. All devices have a channel width W of 10 μm .

L_g (nm)	L_{ch} (nm)	f_T (GHz)	V_{ds} (V)	I_{ds} (mA)	P_{dc} (mW)
75	120	152	0.65	3.07	1.99
120	235	91.4	0.95	2.38	2.26
160	265	67.8	1.05	2.24	2.35
230	340	41	1.15	1.62	1.86
300	450	23.7	1.5	1.30	1.96
420	540	16.5	1.8	1.23	2.22

Table S3. Nominal thermal properties used in simulations. Some thermal boundary conductance (TBC) values not available in the literature were approximated by TBCs for pairs of similar and/or better-studied materials, using the lower bound estimates to model the worst-case scenario. The actual thermal properties vary depending on the material and interface quality, and deposition conditions. The thermal conductivity (TC) of Au as source and drain is lowered due to its thinner film (20 nm), on the other hand, the TC of the Au gate (165 nm) is close to the bulk value (41). We also account for the anisotropic TC of the PI substrate.

Material	TC ($\text{Wm}^{-1}\text{K}^{-1}$)	Material Interface	TBC ($\text{MWm}^{-2}\text{K}^{-1}$)
PI (63-65)	0.2 (Cross-plane) 1.1 (In-plane)	CNT-HfO ₂ and CNT-Al ₂ O ₃ (40, 45, 62, 66, 67)	50
Au (41)	300 (Gate) 150 (Source and Drain)	CNT-Pd/Au (40, 68)	50
HfO ₂ (42)	1.0	HfO ₂ -PI (35, 69)	2.5
Al ₂ O ₃ (42, 43, 70)	1.5	HfO ₂ -Au/Pd (38, 71)	50
CNT (57)	50 (In-plane) 5.7×10^{-4} (Cross-plane)	Al ₂ O ₃ -Al (43, 72)	200
Al (41)	60 (Gate, 20 nm)		